Water Mass Properties Derived From Satellite Observations in the Barents Sea

Benjamin I. Barton, Camille Lique, Yueng-Djern Lenn

JGR Oceans

RESEARCH ARTICLE
10.1029/2019JC015449

Water Mass Properties Derived From Satellite Observations in the Barents Sea

Benjamin I. Barton[1,2,3], **Camille Lique**[1], **and Yueng-Djern Lenn**[2]

[1]Univ. Brest, CNRS, IRD, Ifremer, Laboratoire d'Océanographie Physique et Spatiale (LOPS), IUEM, Brest, France, [2]School of Ocean Sciences, Bangor University, Bangor, UK, [3]National Oceanography Centre, Liverpool, UK

Key Points:
- Satellite data are combined in novel ways to infer steric height in the Barents Sea
- Heat and freshwater contents are estimated from satellite and in situ data from the surface to optimal depths in the central Barents Sea
- Increasing heat content is offset by freshwater content decrease, resulting in no trend in steric height

Correspondence to:
B. I. Barton,
benbar@noc.ac.uk

Citation:
Barton, B. I., Lique, C., & Lenn, Y.-D. (2020). Water mass properties derived from satellite observations in the Barents Sea. *Journal of Geophysical Research: Oceans*, *125*, e2019JC015449. https://doi.org/10.1029/2019JC015449

Received 5 JUL 2019
Accepted 15 JUN 2020
Accepted article online 23 JUN 2020

Abstract The Barents Sea is a region of deep water formation where Atlantic Water is converted into cooler, fresher Barents Sea Water. Barents Sea Water properties exhibit variability at seasonal, interannual, and decadal timescales. This variability is transferred to Arctic Intermediate Water, which eventually contributes to the deeper branch of the Atlantic meridional overturning circulation. Variations in Barents Sea Water properties are reflected in steric height (contribution of density to sea-level variations) that depends on heat and freshwater contents and is a quantity usually derived from in situ observations of water temperature, salinity, and pressure that remain sparse during winter in the Barents Sea. This analysis explores the utility of satellite observations for representing Barents Sea Water properties and identifying trends and sources of variability through novel methods. We present our methods for combining satellite observations of eustatic height (the contribution of mass to sea-level variations), sea surface height, and sea surface temperature, validated by in situ temperature and salinity profiles, to estimate steric height. We show that sea surface temperature is a good proxy for heat content in the upper part of the water column in the southeastern Barents Sea and that freshwater content can be reconstructed from satellite data. Our analysis indicates that most of the seasonality in Barents Sea Water properties arises from the balance between ocean heat transport and atmospheric heat flux, while its interannual variability is driven by heat and freshwater advection.

Plain Language Summary The Barents Sea is an Arctic continental shelf sea where inflowing warm salty water from the Atlantic Ocean loses heat to the atmosphere, gains freshwater from sea ice melt and rivers, and transforms into a water mass called Barents Sea Water. Variability and vertical structure of ocean temperature and salinity can be measured from ships, buoys, and gliders that profile the ocean from surface to bottom but are costly and to some degree limited by sea ice and weather. Satellites observe the ocean more frequently, and cover larger parts of it, but cannot measure below the surface. We combine different satellite measurements with novel physical and statistical techniques to infer ocean heat and freshwater contents, integrated over the upper part of the water column. Using our satellite-based reconstruction of upper ocean heat, we determine that the seasonal ocean heat import is balanced by the warming of the atmosphere by the ocean. These results increase the utility of the available satellite measurements and demonstrate their potential for providing insight that can improve predictions about sea ice and ocean properties in this changing Arctic region.

1. Introduction

The Barents Sea is a gateway for Atlantic Water (AW) entering the Arctic Ocean. There is a net inflow of about 2 Sv of AW through the Barents Sea Opening (BSO) between mainland Norway and Bear Island (Skagseth, 2008). As AW flows through the southern Barents Sea it loses heat to the atmosphere and gains freshwater from net sea ice melt and precipitation, transforming into cooler, fresher Barents Sea Water (BSW) (Ellingsen et al., 2009; Long & Perrie, 2017; Schauer et al., 2002). Once formed, BSW sinks below the fresher Arctic Water (ArW) and flows into the Arctic Basin through St. Anna Trough, making up 50% to 80% of Arctic Intermediate Water (AIW) (Aksenov et al., 2010; Maslowski et al., 2004; Schauer et al., 1997). Between AW and BSW lies the Barents Sea Front. The transition from BSW to the distinctly different salinity-stratified ArW present in the northern Barents Sea is marked by the Polar Front at ~76.5°N (Barton et al., 2018; Loeng, 1991; Oziel et al., 2016). Lique et al. (2010) and Moat et al. (2014) have shown that variability in BSW density impacts the density of AIW exiting the Arctic Basin through Fram Strait, a contributor to the deeper branch of the Atlantic meridional overturning circulation (AMOC).

Since the 1980s, the Barents Sea and Eurasian Basin have become both warmer and saltier (Årthun et al., 2012; Barton et al., 2018; Lind et al., 2018; Morison et al., 2012; Oziel et al., 2016; Polyakov et al., 2017, 2018). This phenomenon, referred to as "Atlantification," occurred along with a decline in winter sea ice cover (Onarheim & Årthun, 2017) and sea ice import into the Barents Sea, resulting in a decrease in freshwater input and a weakening of the ArW-BSW stratification (Lind et al., 2018). A significant increase in the temperature of AW entering the Barents Sea also coincided with a sea ice regime shift in the mid-2000s, increasing the temperature gradient across the Polar Front, limiting the southward extent of winter sea ice, and resulting in warmer and saltier BSW (Barton et al., 2018). The sea ice loss (Hoshi et al., 2019; Petoukhov & Semenov, 2010) and changes in the ocean to atmospheric heat flux (Blackport et al., 2019) in the Barents and Kara Seas have been correlated with anomalous weather conditions in northern Europe, Russia, and Asia. Monitoring the variations and changes in the properties of BSW is thus relevant for understanding the atmospheric and ocean changes, locally in the Barents Sea and beyond.

Steric height is depth-integrated inverse density, resulting from expansion and contraction of the water column due to changes in temperature and salinity (Giglio et al., 2013). The heat and freshwater contents corresponding to the different water masses (AW, ArW, and BSW) are estimated by integrating temperature and salinity across the water mass-specific depth ranges defined by in situ measurements. In general, heat content decreases poleward, as oceanic heat gained at lower latitudes is progressively lost to the atmosphere (Carmack, 2007). This lateral gradient in heat content reaches a threshold within the Barents Sea where density and, hence, stratification become more dependent on salinity than temperature, as water temperature nears the freezing point (Loeng, 1991).

The stratification resulting from temperature and salinity variations can be quantified in terms of α and β, the coefficients for thermal expansion and haline contraction, respectively (Carmack, 2007; McDougall, 1987). The weakly stratified $\alpha-\beta$ transition zones between regions where stratification is dominated by α or β can be classed as "spice-stratified" regions (Stewart & Haine, 2016). The classification between α- and β-dominated regions is important when investigating variations in steric height because of the dependence of steric height on the relative contributions of temperature and salinity to density variability.

In the salinity-stratified, ArW-influenced basins of the central Arctic Ocean and northern Barents Sea, variability in salinity and freshwater content accounts for most of the variability in density and steric height (Armitage et al., 2016). In contrast, along the coast of Norway where the influence of AW is strong, heat content variability dominates the variations in density and steric height in part due to the higher temperatures themselves (Richter et al., 2012) (Figure 1). In the case of BSW, due to the seasonality of heating-cooling and freshwater addition from freeze-thaw, it is possible that BSW is temperature stratified in summer and salinity stratified in winter (Loeng, 1991). As an $\alpha-\beta$ transition zone resides within the Barents Sea, it is equally important to quantify heat and freshwater contents here in order to accurately resolve water mass properties (Figures 1e and 1f). The dependence of steric height on both heat and freshwater contents in the Barents Sea makes it viable for deriving these properties from satellite data, as was pioneered with limited in situ validation by Volkov et al. (2013).

The Barents Sea is reasonably well sampled during the summer season when there is little or no sea ice, whereas it is less accessible in winter when sea ice limits measurements from ships. Argo floats are generally not deployed in the Barents Sea or other sea ice-covered seas. The in situ observations can, however, be combined with satellite observations to improve the temporal and spatial coverage, providing continuous measurements across the region for all seasons. Satellite sea surface height (SSH) measurements of the ocean surface had been obstructed by sea ice (Volkov & Pujol, 2012), but recent advances enable SSH observations in ice-covered areas (Armitage et al., 2016). These satellite altimetry data can be combined with satellite observations of ocean bottom pressure (OBP) to obtain steric height (Armitage et al., 2016; Swart et al., 2010; Volkov et al., 2013). Satellites are also able to measure the sea surface temperature (SST) (Reynolds, 1988) and sea surface salinity (SSS) (Font et al., 2013). At interannual timescales, SST has been linked to depth-integrated heat content in the Barents Sea (Chepurin & Carton, 2012; Lique & Steele, 2013).

In the present analysis, we aim to calculate BSW properties by combining satellite data parameters. Our first objective is to reconstruct the time series of depth-integrated heat and freshwater contents between 2003 and 2013 based on a statistical method applied to satellite data. Second, we examine the interannual variability in BSW and its drivers. We chose the Barents Sea as a test site for this study due to the relatively large collection

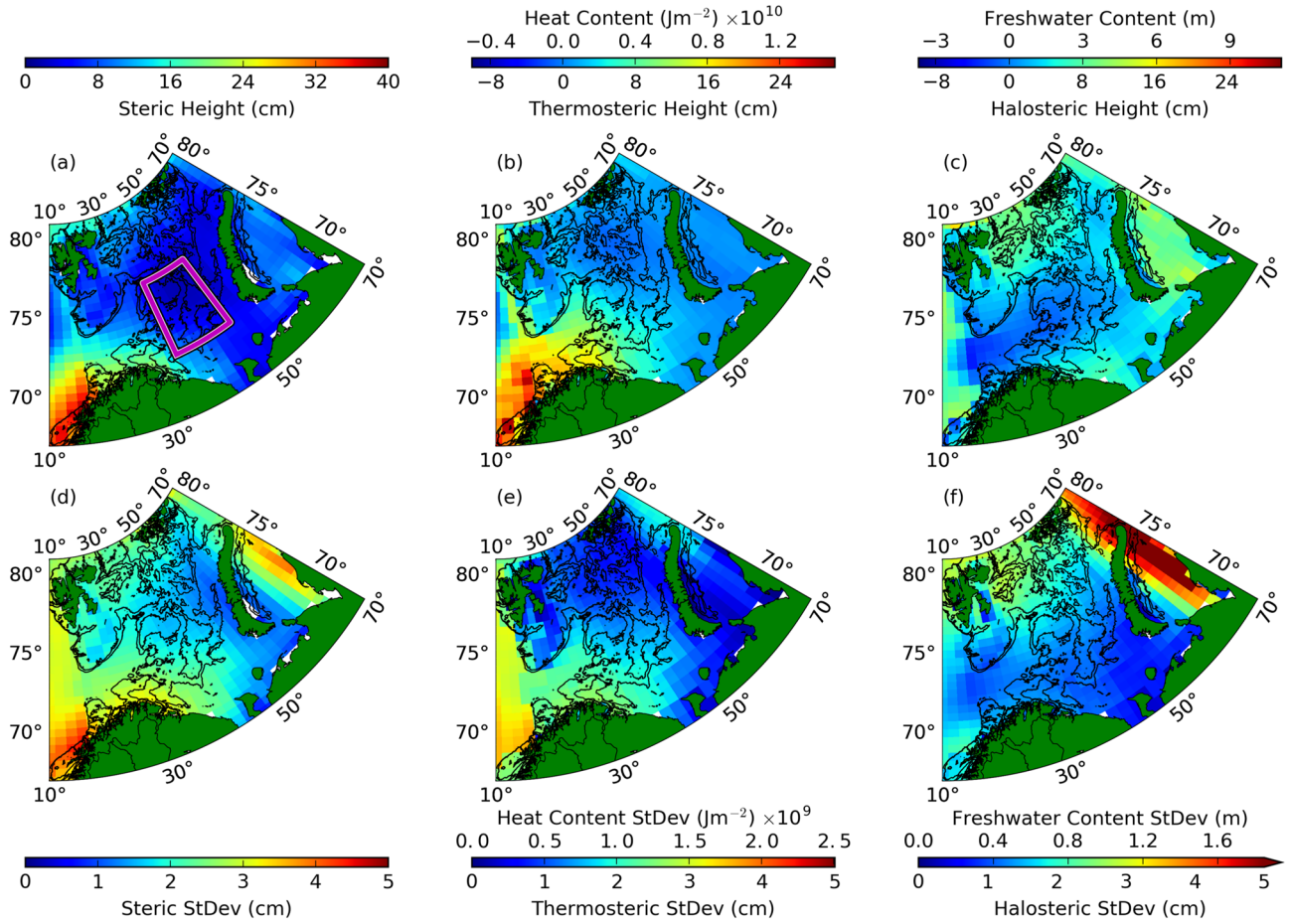

Figure 1. Average over 2003–2013 and estimated for the whole water column (a) in situ steric height, (b) in situ heat content and in situ thermosteric height, and (c) in situ freshwater content and in situ halosteric height estimated from EN4. (d)–(f) show the standard deviation of in situ steric height, heat content, thermosteric height, freshwater content, and halosteric height, estimated from the monthly means. The purple box in (a) shows the Central Box, covering the Central Basin and Central Bank, where the time series are averaged over for investigations of BSW variability (see section 4). Black lines show the 220 and 300 m isobaths.

of historic hydrographic profiles (Oziel et al., 2016). This study further focuses on the formation region of BSW, a precursor to AIW. This region is identified by the Central Basin (Oziel et al., 2016; Schauer et al., 2002) and defined in this study by a box encompassing the Central Basin referred to as the Central Box (purple box Figure 1). The data and methods will be presented in sections 2.1 and 2.2, the first objective will be evaluated in section 3, the second objective will be evaluated in section 4, and the conclusions from the paper will be presented in section 5.

2. Data and Methods

2.1. Data

We used satellite-derived SSH, OBP, and SST to estimate steric height and heat and freshwater contents, which was then verified using in situ observations. In this section we describe the data sets and detail the methods used.

Data on SSH were provided by the Centre for Polar Observation and Modelling (CPOM) (Armitage et al., 2016). To obtain SSH everywhere in the Barents Sea, including under sea ice, a processing technique has been applied to satellite altimeter data that takes into account the difference in character of satellite echo-return signals from specular surfaces (ocean between leads) and nonspecular surfaces (snow and sea ice) (Giles et al., 2012; Laxon, 1994). The product has previously been used to examine Arctic Ocean circulation (Armitage et al., 2017; Regan et al., 2019). The data are monthly from January 2003 to December 2013

with a resolution of 2° longitude by 0.5° latitude (58 × 56 km in the Barents Sea) and an estimated uncertainty of 1.1 cm (Armitage et al., 2016).

The twin Gravity Recovery and Climate Experiment (GRACE) satellites measured time-varying OBP through changes in Earth's gravity anomalies (Wahr et al., 1998). OBP is determined by removing the local, atmospheric, inverted barometer effect from the measured mass-induced pressure (Peralta-Ferriz et al., 2014). Converting OPB in decibels to a depth of water in meters and further subtracting the tide gives the eustatic height variability (the contribution of dynamics in water mass to sea-level variations). We used gridded eustatic height, corrected for atmospheric pressure and tides from the GRCTellus Ocean monthly data set, available from August 2002 to December 2016 (Version RL05.DSTvDPC1401, downloaded from ftp://podaac-ftp.jpl.nasa.gov/allData/tellus/L3/ocean_mass/RL05). This data set is the ensemble mean of the three solutions provided by Center for Space Research (CSR), Jet Propulsion Laboratory (JPL), and Geoforschungs Zentrum Potsdam (GFZ), as suggested by Sakumura et al. (2014). This specific data set has been previously used for Arctic studies by Peralta-Ferriz et al. (2014, 2016).

Data are provided at 1° grid spacing with 500 km Gaussian smoothing applied (for comparison Novaya Zemlya is ~800 km long). The estimated root-mean-square error (RMSE) for each of the ensemble members is 1.5–2 cm at high latitudes (Chambers & Bonin, 2012; Peralta-Ferriz et al., 2016). Using the ensemble mean decreases the RMSE by at least 0.3 cm, resulting in an RMSE of 1.2 cm in the Barents Sea (Sakumura et al., 2014). This data set has been validated with both altimetry and Argo floats globally (Chambers & Willis, 2010) and with in situ OBP sensors in the Arctic Ocean, the Barents Sea, and Kara Sea (Peralta-Ferriz et al., 2016).

We also used satellite SST data from the OSTIA project spanning 1985 to present (Donlon et al., 2012) (downloaded from http://marine.copernicus.eu/services-portfolio/access-to-products/?option=com_csw&view=details&product_id=SST_GLO_SST_L4_NRT_OBSERVATIONS_010_001). This data set is optimally interpolated from multiple satellite sensors together with in situ observations onto a 0.05° grid (1.5 × 5.6 km for the Barents Sea) at a daily frequency. The data set is able to resolve features at spatial scales greater than 10 km, and the accuracy is ~0.57 K (Donlon et al., 2012), but cannot resolve mesoscale variability (with a characteristic scale of only a few kilometers) in the Barents Sea, although the resolution does show fronts in the region (Barton et al., 2018).

Temperature and salinity fields from the EN4 data set were used for evaluating the satellite data (EN4.2.0, www.metoffice.gov.uk/hadobs/en4). EN4 comprises in situ ship CTD profile data and Argo float data optimally interpolated on a 1°, monthly z grid with 42 levels (Gouretski & Reseghetti, 2010). Data are available from January 1980 to December 2016. Within the Barents Sea (10°E to 65°E and 68°N to 80°N) over this time frame, every 3 month period has more than 117 profiles with a total of 33,323 profiles in this region during our study period. These profiles are biased toward September, October, and November when there are usually more than 400 profiles, and there is a spatial bias in favor of the southwestern Barents Sea.

The fields of surface heat flux, evaporation, and precipitation from the ECMWF ERA-Interim reanalysis were used to investigate the drivers of the interannual variability in BSW properties (Berrisford et al., 2011; www.ecmwf.int). This data set is provided on a 0.75° grid (84 × 16 km for Barents Sea) with 3-hourly temporal resolution, averaged into monthly means. Data are available from January 1979 to December 2018. The atmospheric fluxes are spatially averaged within the purple box in Figure 1, and interannual variability is found using a simple 12 month running mean. Note that a 12 month running mean filter allows some annual signal to remain in the data but is adequate for resolving the timescales of interest to us.

Bathymetry was taken from the GEBCO 2014 30 arcsecond resolution data set (Weatherall et al., 2015; GEBCO_2014 Grid, Version 20150318, www.gebco.net). In the Barents Sea, it corresponds to a grid of 0.2 km in longitude and 0.9 km in latitude.

In the following analysis, we focused on the period when all the observational data sets are available, January 2003 to December 2013. EN4, GRACE, OSTIA, and ECMWF data were linearly interpolated on the same grid as the CPOM SSH. By default, GRACE data are masked around land. Before interpolation onto the CPOM SSH grid, we extrapolated GRACE data spatially toward the coastal areas by one grid cell using weighted averaging of the nearest neighbors. This is reasonable given that GRACE data have a 500 km filter.

2.2. Methods

Steric height can be calculated using three methods: (i) from SSH and eustatic height (Armitage et al., 2016), (ii) from halosteric and thermosteric heights (Gill & Niiler, 1973; Volkov et al., 2013), and (iii) through the integration of in situ density (Roquet et al., 2015). Here, we regarded steric height derived from integrating EN4 data as the ground-truth data for validating the satellite-inferred estimates. Thermosteric and halosteric heights can also be derived from temperature and salinity profiles and are statistically proportional to heat and freshwater contents (Steele & Ermold, 2007). We converted heat and freshwater contents to halosteric and thermosteric heights, giving us parameters with the same units as steric height (in m). We used the following methods, largely based on previous work for estimating the various components of SSH. Our additions to this were deriving the equations to convert heat content to thermosteric height, and freshwater content to halosteric height, as detailed below.

2.2.1. Satellite Steric Height

Obtaining steric height from satellite data was done using the following equation (Armitage et al., 2016):

$$\eta_{st} = \eta_H - \eta_m \tag{1}$$

with η_{st} the steric height, η_H the SSH, and η_m the eustatic height.

In addition, we obtained steric height from in situ profiles using the integral of specific volume anomaly from a reference pressure for comparison to satellite data (i.e., the dynamic height anomaly) (Roquet et al., 2015).

$$\eta_{st}(t) = \frac{1}{g}\int_{p_2}^{p_1} \frac{1}{\rho(z,\ t)} - \frac{1}{\rho_{\mathrm{ref}}(z)}\, dp \tag{2}$$

with g the gravity taken as 9.7963 m s^{-2}, p_1 and p_2 the ocean surface and bottom pressures in Pa, $\rho(z, t)$ the density as a function of depth and time, and $\rho_{\mathrm{ref}}(z)$ a reference density calculated for $T = 0$°C and $S = 35$ with variable pressure. This was calculated using the Gibbs Sea Water function package (http://www.teos-10.org/pubs/gsw/html) (IOC et al., 2010).

2.2.2. Thermosteric and Halosteric Height

Steric height can be defined as a function of thermosteric (η_T) and halosteric (η_S) heights, each of which can be calculated directly from integration of in situ profiles (Gill & Niiler, 1973). In the following equations, overhat (e.g., $\hat{\rho}$) indicates averaging over depth, while overbar (e.g., $\overline{T}$) indicates averaging in time:

$$\eta_{st} = \eta_T + \eta_S + \overline{\eta_{st}} \tag{3}$$

Following (Lind et al., 2018), we define heat content as

$$H(t) = \rho_0 C_p \int_{h_2}^{h_1} T(z,\ t)dz \tag{4}$$

with H as heat content, ρ_0 as reference density (here taken as the spatiotemporal mean), C_p as heat capacity of seawater (here taken as 3,985 J kg^{-1} K^{-1}), h_1 and h_2 the ocean surface and bottom depth in m, and $T(z,t)$ as temperature in °C as a function of depth and time.

In this paper, we derived thermosteric height from heat content using the following equation:

$$\eta_T(t) = \hat{\overline{\alpha}}\left(\frac{H(t)}{\rho_0 C_p} - \int_{h_2}^{h_1} \overline{T}(z)dz\right) \tag{5}$$

where $\hat{\overline{\alpha}}$ is the coefficient of thermal expansion averaged over time and depth.

Freshwater content, F, used by Lind et al. (2018) was defined as

$$F(t) = \int_{h_2}^{h_1} \frac{S_r - S(z,\ t)}{S_r}\, dz \tag{6}$$

where $S(z, t)$ is salinity as a function of depth and time. As we estimated steric height relative to $T = 0$°C

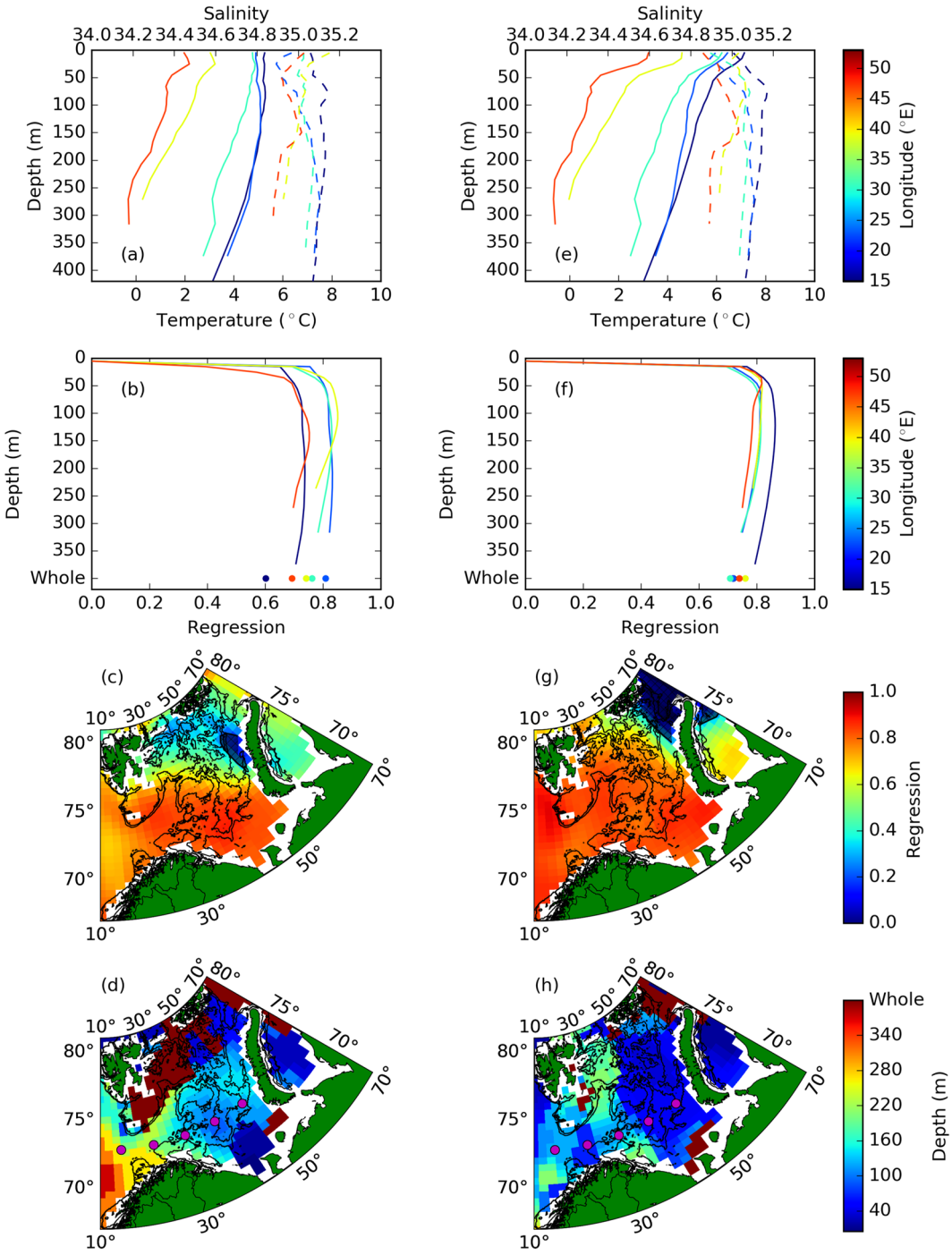

Figure 2. (a) Climatology $T-S$ profiles from EN4 for winter (October to March). Solid line is temperature, and dashed line is salinity. The color shows the location of the profile along the purple dots at 72.5°N shown in (d). The 72.5°N profiles are an example of the transition from AW to BSW. (b) Regression of satellite steric height with EN4 steric height between various integration depths and the surface for winter (October to March). The color shows the location of the profile along the purple dots at 72.5°N shown in (d). (c) Regression of satellite steric height with EN4 in situ steric height between optimum integration depth (OID) and the surface for winter. Hatching shows areas with significance <99%. (d) Spatially varying OID used in (c). The depth "Whole" on axes refers to integration over the whole water column. White, coastal areas show where data are not available. (e)–(h) are the same as (a)–(d) but for summer (April to September). Black lines show the 220 and 300 m isobaths.

and $S = 35$, freshwater content is also estimated relative to reference salinity S_r where $S_r = 35$. Similar to thermosteric height, in this paper, we derived halosteric height from freshwater content:

$$\eta_S(t) = \hat{\bar{\beta}}\left(-F(t)S_r + \int_{h_2}^{h_1} S_r - \overline{S}(z)dz\right) \tag{7}$$

where $\hat{\bar{\beta}}$ is the coefficient of haline contraction averaged over time and depth.

We applied these equations to the data, allowing us to compare satellite steric height calculated using Equation 1, with in situ steric height calculated from EN4 data using Equation 2. Thus, to avoid confusion, hereafter, quantities will be prefixed by satellite or in situ respective to the source of data they were derived from. Note that the satellite steric height is noisier than the in situ steric height due to inherent noise in the two satellite products used to calculate it. To account for this and to focus on timescales that are likely to be resolved in the different data sets, we smoothed the data with a 3 month running mean. Consequently, our methods can account for seasonal variability but will not resolve higher-frequency variability.

To account for the spatial variability in the Barents Sea, we calculated properties at each individual grid point of the interpolated data sets. The in situ steric height was calculated from the surface downwards to each depth. We regressed in situ steric height at each depth against satellite steric height. We identified the optimum integration depth (OID) from the maximum regression value at each grid point (Figure 2). The OID has a strong seasonal dependence that can be divided into a "strong-stratification" summer season (April to September) when OID heat content shallows and "weak-stratification" winter season (October to March) when the OID deepens. The OID was fixed for these summer and winter seasons but is a function of location. A complete discussion of the roots of this seasonal and spatial variability follows in section 3.

2.2.3. Statistical Model for Satellite-Based Heat and Freshwater Contents

In line with the first objective of the study, we compared estimates of EN4-based heat content, integrated between the surface and the seasonally dependent OID, with SST (Figure 3). We derived a statistical model to determine heat content from SST for each of the summer and winter seasons. The sea ice-covered season was not treated separately because this was accounted for in the data set where SST was set to -1.8 under sea ice. Our linear regressions were calculated using least squares regression of monthly data with significance estimated at the 99% level using a two-tailed Student's t test. Effective degrees of freedom were estimated from the decorrelation timescale ($1/e$ of peak correlation) required to avoid autocorrelation. The effective degrees of freedom were used in significance estimates and in calculating standard error. We performed the same method to produce a SSS-to-freshwater content model using EN4 freshwater content and SSS from the top layer (0 to 10 m depth) in EN4.

3. Evaluation of Water Properties Derived From Satellite Data Sets

In this section we address the first objective of estimating water properties from satellite data. We begin our discussion by reviewing the distribution of steric height and freshwater and heat contents resolved by in situ observations in the Barents Sea. We then discuss the nuances of applying the methods outlined in the previous section to calculate satellite steric height and show how these methods perform by comparing them with in situ estimates. This analysis is carried out on the whole Barents Sea rather than just the Central Box.

3.1. In Situ Properties

Several water masses exist in the Barents Sea, with temperature and salinity decreasing from southwest to northeast, each with variable impact on in situ steric height. To quantify these spatial changes, we calculate in situ steric height using Equation 2 integrated over the whole water column (Figure 1). At the entrance of the Barents Sea at 19°E, in situ steric height is on average 0.2 m, in situ heat content is 0.9×10^{10} J m^{-2}, and in situ freshwater content is 0 m (Figures 1a–1c). Within the southwestern Barents Sea, mean in situ heat content and steric height decrease to minima of 0.03 m and 0.2×10^{10} J m^{-2} at 40°E in the Central Basin. Mean in situ heat content remains around 0.2×10^{10} J m^{-2} both northward and eastward of the Central Basin, while mean in situ freshwater content increases from 0 m in the Central Basin to 3 m in the northern Barents Sea, dominated by fresher Arctic Water.

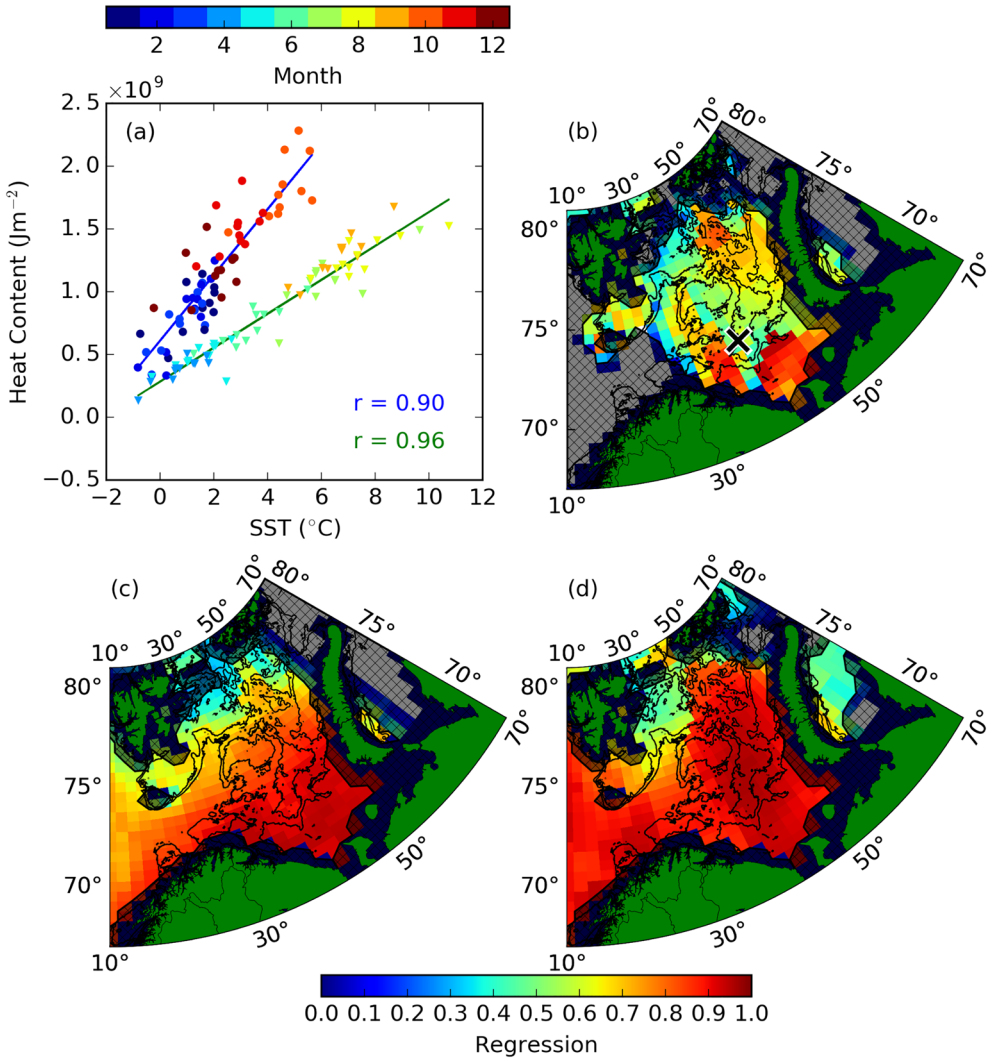

Figure 3. (a) Regression of satellite SST with EN4 in situ heat content at a single point in the Barents Sea, marked with a black cross in (b). Satellite SST is regressed against EN4 in situ heat content calculated to the optimum integration depth (OID) shown in Figures 2c and 2f. Blue line and circles show winter season, and green line and triangles show strong-stratification season. Regression of satellite SST with EN4 in situ OID heat content using (b) a one model system, (c) the winter model (October to March), and (d) the summer model (April to September). Hatching on maps shows areas with significance <99%. Black lines show the 220 and 300 m isobaths.

The temporal standard deviation of monthly mean in situ steric height varies between 0.01 and 0.03 m across the Barents Sea (Figure 1). This is smaller than the annual cycle amplitude of satellite steric height identified as varying between 0.06 and 0.01 m by Volkov et al. (2013). Both the lowest standard deviation and the smallest mean steric height are found in the eastern Barents Sea. In the southwestern Barents Sea, the standard deviation in both in situ steric and thermosteric height is ~0.025 m, while the standard deviation in the in situ halosteric contribution to steric height is ~0.01 m. These are comparable to the results of Volkov et al. (2013), who found the amplitude of thermosteric height as 0.012 m and halosteric height as 0.006 m in the Barents Sea for 1980 to 1995. In the Central Basin, the standard deviation in in situ thermosteric height decreases to 0.02 m, while the standard deviation in in situ halosteric height increases to 0.015 m, showing that the standard deviation in in situ steric height arises almost equally from variability in in situ freshwater and heat contents. These results agree with Volkov et al. (2013). In the northern Barents Sea, the standard deviation in in situ thermosteric height is 0.01 m, but both the in situ steric and halosteric standard deviations are ~0.02 m, confirming that the variability in in situ freshwater content contributes more to the variability in in situ steric height, than variations in in situ heat content, as expected for the cold, salinity-stratified

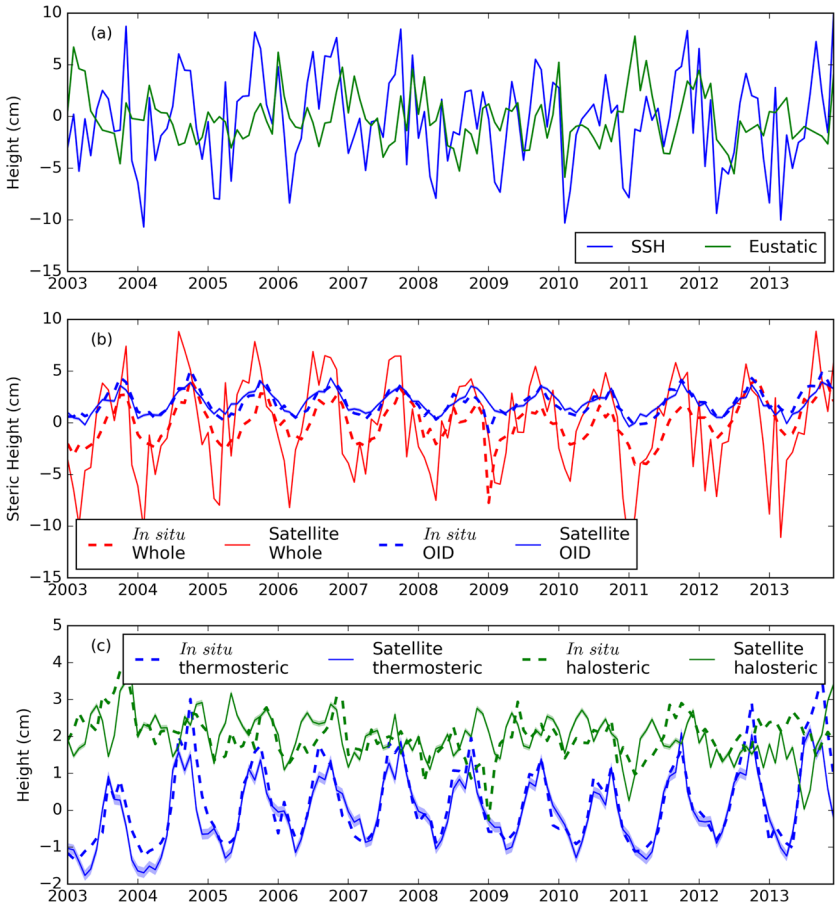

Figure 4. Time series at the point marked with a black cross on Figure 3b of SSH and GRACE eustatic height (a), EN4 in situ steric height integrated between the surface and bottom (b, dashed red line), EN4 in situ OID steric height for the upper water column indicated by the integration depths in Figures 2d and 2h (b, dashed blue line), satellite steric height for the whole water column (b, solid red line), and satellite OID steric height smoothed with a 3 month running mean (b, solid blue line). In situ OID thermosteric and halosteric heights estimated for the upper water column and satellite OID thermosteric and halosteric heights for the same depth range (c, note that the halosteric height has been offset by +2 cm for clarity). Standard error bars are shown by shading.

northern Barents Sea (Figures 1e and 1f). This is consistent with Stewart and Haine (2016), who showed the Barents Sea as a region where vertical instability could occur. Vertical instability is where the water column has denser water above lighter water and would be likely to coincide with brine rejection during sea ice formation at the surface. Vertical instability could also occur where warmer, saltier AW is subject to intense surface cooling during winter. This would place cold saltier water on top of a previous year's fresher BSW (Figures 2a and 2b). The transition from AW to BSW is found in the climatology temperature and salinity profiles from west to east showing this spatial transition in properties occurs throughout the water column (Figures 2a and 2e).

3.2. Satellite Steric Height

Satellite-based estimates of steric height, thermosteric height, and halosteric height were computed by applying the methods of section 2.2. To illustrate model skill, we use a single location in the Central Basin (shown by the black cross in Figure 3b) where satellite steric height is highly correlated with the wider Barents Sea (not shown). The satellite SSH and eustatic height data at this location each shows high-frequency variability (Figure 4a). In situ observations integrated from surface to bottom should theoretically reproduce the satellite-observed steric height, but our analysis shows that this is not always the case. Our initial calculation of satellite steric height produced a result that overestimates the in situ steric height

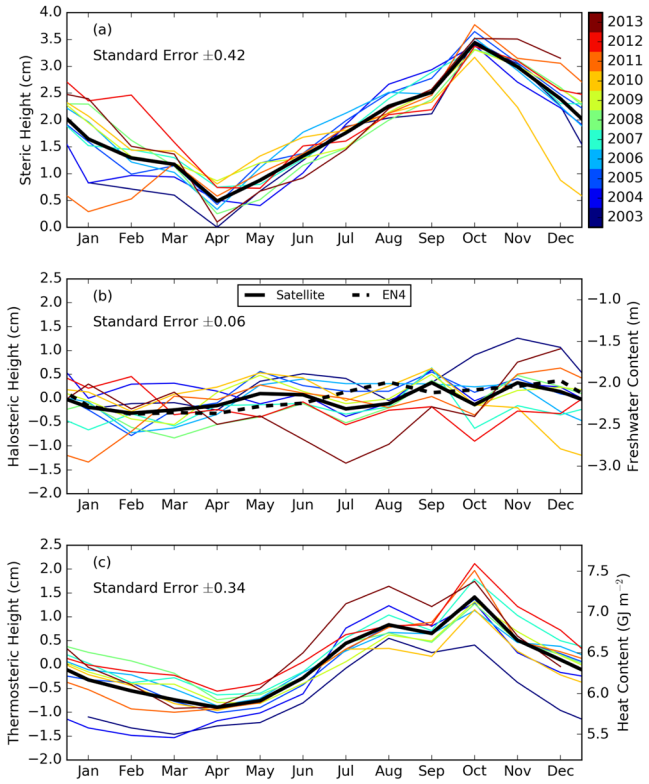

Figure 5. Mean seasonal cycle (thick line) and interannual variability (colors indicate individual years) of satellite OID steric height (a), satellite OID halosteric height (b), and satellite OID thermosteric height (c) averaged over the Central Box (purple box in Figure 1). (b) Dashed line shows in situ OID halosteric height climatology. Standard error for the interannual variability in the seasonal cycle is shown.

(red lines Figure 4b). Part of this overestimation arises from a seasonal bias. Indeed, the climatologies of satellite and in situ steric height have different timing in their seasonal cycle. Satellite steric height seasonal cycle peaks in September, while the in situ cycle peaks in October. In October, in situ observations show that surface mixed layer thickness has passed its September peak and is eroding while the deeper water column is increasing in thickness (not shown). This implies that satellite steric height variability is most sensitive to and, hence, is representative of the upper ocean steric height, rather than the full water column. This is the stronger signal in steric height where water mass transformation is occurring (Figure 5). Another issue that could cause the overestimation is the seasonal bias in hydrographic profile collection.

Thus, in order to account for the difference in satellite and in situ steric height climatology, we have split the data set into two seasons: a "strong-stratification" season (summer, April to September) and a "weak-stratification" season (winter, October to March). Summer mixed layer depth in the AW region of the Barents Sea reaches 50–60 m and mixes downward in winter, homogenizing to 200–300 m depth (Loeng, 1991; Smedsrud et al., 2010). This seasonal change in surface layer properties can be seen in the climatology of EN4 $T-S$ profiles (Figures 2a and 2e). The mixed layer in the northern Barents Sea influenced by ArW reaches 20–40 m in summer and mixes down to 100–150 m in winter (Lind et al., 2018; Loeng, 1991; Smedsrud et al., 2010). EN4 data show similar seasonally varying depths for stratification (Figures 2a and 2e). In addition, the EN4-inferred mixed layer in the Central Basin (where BSW is formed) is ~50 m in summer and ~150 m in winter. This means that the variability in satellite steric height is expected to be representative of a larger depth range of the water column during the winter than during the summer, when the deeper part of the water column is isolated from direct surface interaction. Splitting the data sets between these two seasons was an appropriate compromise between improving the model with known physical processes and not biasing the satellite data to the scarce in situ winter data, which is often based on <3 profiles in the Central Basin.

Having split the data according to season, we regressed the satellite steric height against in situ steric height calculated between the surface and a range of integration depths (Figures 2b and 2f). The maximum regression of satellite and in situ steric height depends on both the location and the depth range over which in situ steric height is integrated. The OID (depth with the largest r value) is significant because this essentially captures the depth range over which water mass transformation is occurring within each season. However, the OID and mixed layer depths are not the same, since the mixed layer depth evolves over the summer and winter seasons while we only use one integration depth per season. During winter, the OID shoals eastwards from >250 m in the western Barents Sea to 120 m in the Central Basin (Figure 2c). The shallower OID in the Central Basin is similar to the depth where "doming" of pycnoclines was observed by Ozhigin et al. (2000) and (Schauer et al., 2002), which is likely a signature of the ventilation of isopycnals and the formation of deep water. The OID is also similar to the mixed layer depths found in the model analysis by Aksenov et al. (2010). During the summer season, the OID ranges between 50 and 150 m across the south and eastern Barents Sea (Figure 2h).

Across the southern Barents Sea, regressions between in situ and satellite OID steric heights for both seasons are around 0.8, while in the northern Barents Sea, the regression drops to around 0.4 during the winter (Figures 2c and 2g). The seasonal sea ice cover in the north results in a very limited number of profiles during winter and spring, so that EN4 only reflects the long-term seasonal climatology in this region during winter and spring. This could be a factor in explaining the lower regression values between in situ and satellite OID steric height measurements found in this region. Inaccuracy introduced to SSH from sea ice could also contribute to lower regression values. It is likely that the regression could be improved further by carefully

weighting both the in situ and satellite data for the northern Barents Sea in winter. However, since this study is focused on the BSW formation zone in the Central Basin, we have selected a biseasonal approach that is robust for our region of interest.

We estimated the uncertainty of the satellite OID steric height to determine the quality of the measurement and how far they may deviate from the true value. The uncertainty of the satellite OID steric height was estimated from the uncertainties of the component data sets, OBP and SSH, using quadrature combination of uncertainty. This was applied to Equation 1 as $\Delta_{\eta_{st}} = \sqrt{m(\Delta^2_{\eta_H} + \Delta^2_{\eta_m})}$ where Δ is the respective uncertainty of η_{st} (steric height), η_H (SSH), and η_m (eustatic height). m is the regression model gradient. We find that the conservative estimate of uncertainty of our satellite product of OID steric height is 1.0 cm, comparable to the 1.9 cm uncertainty of Armitage et al. (2016).

3.3. Satellite Heat and Freshwater Contents

Determining the water column properties from surface satellite observations requires a robust statistical relationship between satellite SST and in situ heat content, similar to that proposed from model analysis by Lique and Steele (2013). In order to infer satellite OID heat content from satellite SST, we combine two statistical models corresponding to our summer and winter, determined by regressing in situ OID heat content against satellite SST for each grid point. Figure 3a shows how the satellite SST and in situ OID heat content gradually increase through the summer, from April to September. At our illustrative location (cross in Figure 3b), satellite SST decreases between September and October, but the in situ OID heat content increases due to deepening of the mixed layer (Kantha & Clayson, 1994; Loeng, 1991) (Figure 3a). From October to March, satellite SST declines linearly with in situ OID heat content. Given the 0.57 K uncertainty associated with the satellite SST product, the uncertainty is propagated with the regression gradient for heat content (similar to the satellite OID steric height uncertainty) to give an uncertainty in satellite OID heat content of 4×10^8 J m^{-2}.

Figures 3b–3d show the skills of the regression models geographically. Both the summer and winter models have greater regression values than a single regression model independent of season. Each of the summer and winter regression models shows r values greater than 0.8 throughout the southern Barents Sea and greater than 0.9 in the Central Basin. In the northern Barents Sea, the winter model is less effective, with regression values varying between 0.3 and 0.7 (Figure 3c). The satellite SST to OID heat content model differs from the steric height regression in regions with seasonal sea ice. The northern Barents Sea is seasonally covered by sea ice. When sea ice is present, satellite SST is relatively constant at -1.8°C (although the date of the onset of freeze and melt may vary from year to year), making satellite SST less representative of the in situ OID heat content.

The same method can be applied to derive a statistical model estimating in situ OID freshwater content from in situ SSS. Ideally this analysis would have been carried out with satellite SSS instead of EN4 data. Retrieving SSS from L-band measurements at high latitudes (i.e., in cold water) is known to be particularly challenging (Olmedo et al., 2018). A quick comparison between the EN4 SSS and different satellite SSS products during their respective overlapping periods revealed that, while the mean spatial patterns are similar in sea ice-free regions, satellite SSS products are unable to reproduce the temporal variability found in EN4 SSS (not shown). This implies that our analysis for satellite halosteric height (detailed in the next paragraph) could be used to expand and improve the satellite SSS record over a longer period, starting in 2003. Therefore, we assume that in situ SSS is best represented by the first depth bin (0 to 10 m depth) of the EN4 salinity field. We acknowledge that a better in situ SSS-to-OID freshwater content fit is expected as we are making comparisons within one data set (EN4), in contrast to the satellite SST to OID heat content model for which data from independent sources were considered. Accordingly, the in situ SSS-to-OID freshwater content model at our illustrative location shows that SSS is representative of freshwater content in the upper water column (Figure 6a). There is a smaller difference between the summer and winter seasons and less dependence on the month considered than the satellite SST to OID heat content model. Regression values for the SSS-to-OID freshwater content model are around -0.9 at the 99% significance level across the northern and eastern Barents Sea in the summer season (Figures 6b–6d). The winter has regression values between 0.5 and 0.9, with the greater values found in the western Barents Sea. This shows that our satellite OID freshwater content has potential to be a novel estimate of SSS.

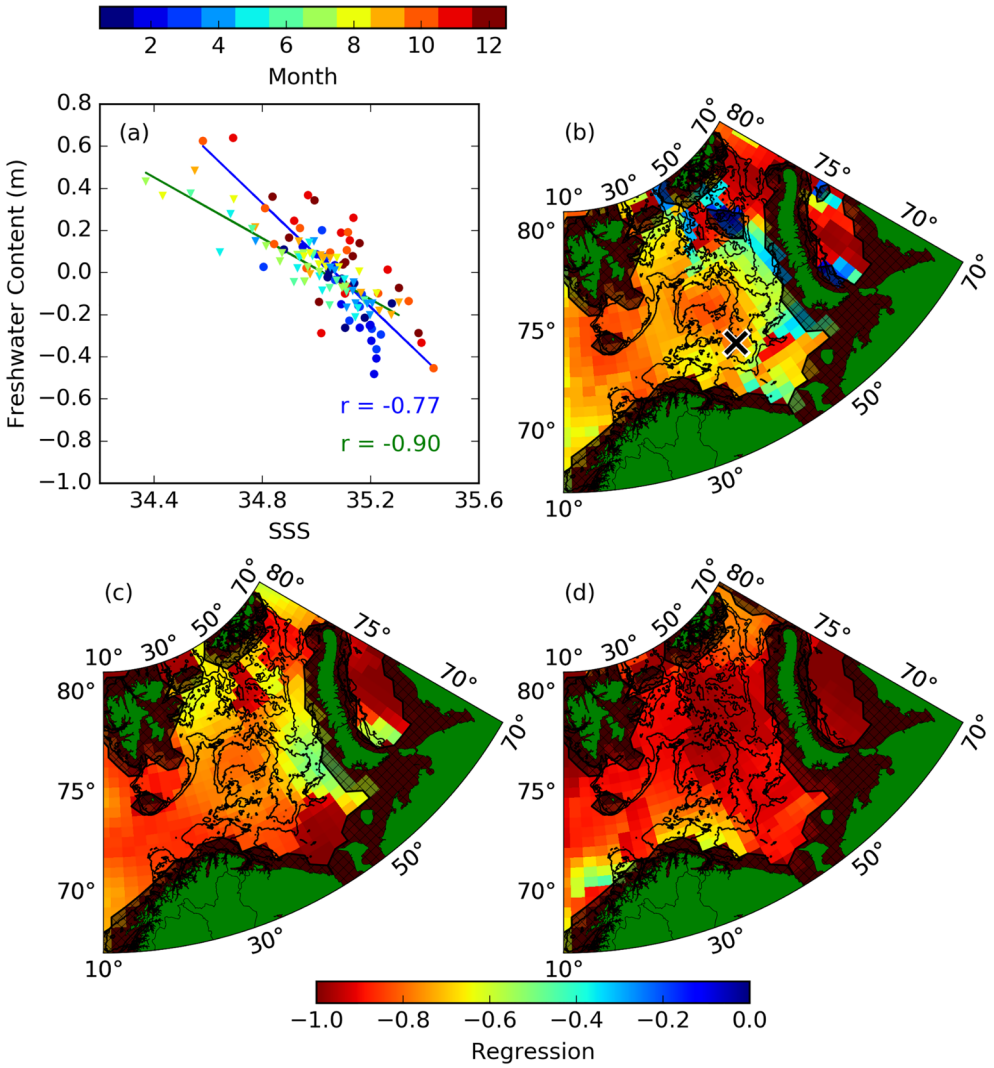

Figure 6. Same as Figure 3 but for EN4 in situ SSS and EN4 in situ OID freshwater content.

Using satellite OID steric height and satellite OID thermosteric height estimated from heat content with Equation 5, we use Equation 3 to estimate the satellite OID halosteric height (the reconstruction for our example location is shown in Figure 4c). The ability of the satellite model to retrieve an accurate OID halosteric height time series is significant, with regression values with the in situ OID halosteric height between 0.4 and 0.55 in the Barents Sea (significant at the 99% level) (Figure 7). Although the regression is not strong it shows that satellites can nevertheless provide information about OID halosteric height variability. There are only a few EN4 profiles in the Kara Sea making the data sets here more representative of the climatology in this region. When satellite OID heat content is converted to satellite OID thermosteric height, thermosteric height has an uncertainty of 1.1 cm. Using quadrature uncertainty combination of the satellite OID steric height and thermosteric height, the uncertainty of the estimated satellite OID halosteric height is 1.5 cm and the uncertainty of satellite OID freshwater content is 0.6 m. For this study we note that the gridded EN4 data set does capture the variations of the water mass properties but that the irregular sampling, particularly during winter and spring, means that temporal inaccuracies are inevitable. Individual $T-S$ profiles used in producing the gridded EN4 product can also be biased by mesoscale features that are not resolved in the satellite data. Figure 7 suggests no significant regression between satellite and in situ OID halosteric heights in the Norwegian Sea. We speculate that this was caused by reduced dependence of densities on salinity due to greater temperature here, resulting in a smaller halosteric contribution to satellite and in situ steric height, as shown by the standard deviation in Figures 1c and 1f.

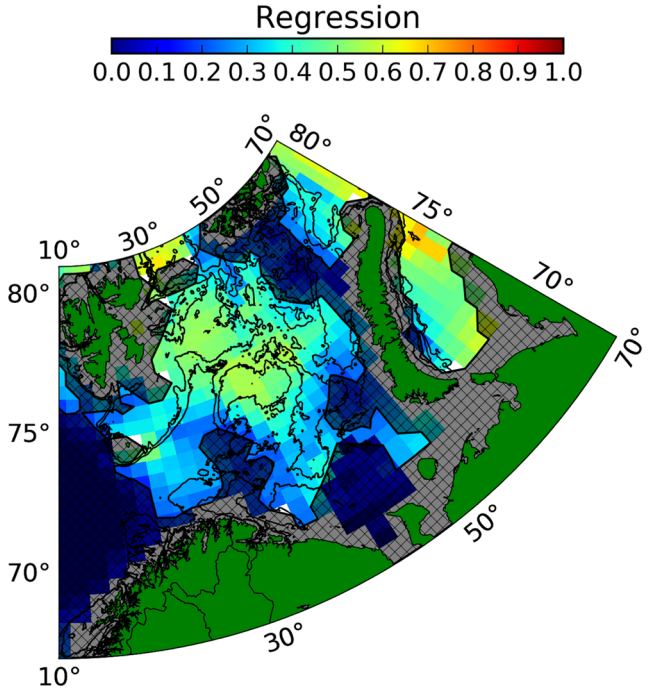

Figure 7. Regression of satellite optimum integration depth (OID) halosteric height with EN4 in situ OID halosteric height. Hatching shows areas with significance <99%. White, coastal areas show where data are not available due to limitations of GRACE data. Black lines show the 220 and 300 m isobaths.

The limitations of OID steric, thermosteric, and halosteric heights reconstructed here are inherited from their components, but the satellite-based analysis allows us to fill in gaps. The EN4 profiles have irregular spatial and temporal resolution, GRACE has a 500 km low-pass filter, SSH may be more noisy in sea ice-covered areas, and SST has a constant value in sea ice. By combining SST and EN4, satellite OID thermosteric height is expected to have a similar spatial scale to EN4, and the temporal feature resolution is monthly in sea ice-free areas. The steric height and halosteric height are both limited by the 500 km spatial feature resolution of GRACE, and temporal feature resolution is seasonal. Halosteric height will be more limited by sea ice than steric height because of its reliance on SST. The satellite data have lower accuracy than EN4 and do not offer information on vertical structure. The satellite data give information on the OID and assume a seasonally dependent OID depth for each location. These data should be used as complementary to EN4 or other profile data sets.

4. Understanding the Variability of BSW

In this section we explore the seasonal and interannual variability in thermosteric and halosteric heights. The satellite-derived, upper ocean OID properties show similar spatial patterns in the mean and standard deviation to the whole water column in situ data (Figures 1 and 8). The key features are the signature of warm AW entering the Barents Sea from the west in the satellite OID heat content, which cools as it passes through the Barents Sea and causes a minimum in mean satellite OID steric height as it reaches the Central Basin (Figures 8a and 8b). The Central Basin has been suggested as the BSW formation region (Loeng, 1991; Oziel et al., 2016). In the Central Basin, satellite OID freshwater content is greater than the western Barents Sea but is less variable (Figures 8c and 8f).

Satellite OID thermosteric and halosteric heights have some spatial coherence within the Central Basin due to the coherence in the EN4 and GRACE measurements. Therefore, all values are averaged within a representative box for BSW defined by 35°E to 47°E and 71°N to 76°N (~400 × 550 km box; see Central Box on Figure 1). This box lies between the Polar Front at 76.5°N, the Barents Sea Front at ~35°E, and the Coastal Water Front that roughly runs along 71°N between 33°E and 50°E and along 50°E between 72°N and 76°N (Barton et al., 2018; Oziel et al., 2016). The Central Basin has previously been identified as a convective BSW formation site in model analysis (Aksenov et al., 2010); therefore, we consider that the quantities averaged within this box are indicative of the BSW properties. Note that all ERA-Interim atmospheric fluxes presented here are also averaged within this box, but the sea ice cover refers to the whole Barents Sea as our box was mostly ice free from 2005 onwards (Barton et al., 2018). Even though sea ice is not present, the melt water can still be advected into the box and is a regional freshwater source that would not be found entering the BSO.

There is a pronounced seasonal cycle in the satellite OID steric height, with a maximum in October and a minimum in April (Figure 5). In our Central Basin box, the timing of the summer and winter extrema of the satellite OID steric height corresponds to the seasonal variability in thermosteric height (see section 3 and Figure 3). An examination of the interannual variability in satellite OID steric height reveals a shift in the seasonal cycle over time (Figure 5). Interannually, June, July, and October satellite OID halosteric height each decline at -0.070, -0.095, and -0.105 cm year^{-1}, respectively (significant at 95% level, 0.03 cm standard error). The interannual trend in each of May, June, and October satellite OID thermosteric height is 0.055, 0.072, and 0.103 cm year^{-1}, respectively (significant at 95% level, 0.01 cm standard error) over the whole time period. The lack of significant trend in individual months for satellite OID steric height is likely due to opposing trends in thermosteric and halosteric heights.

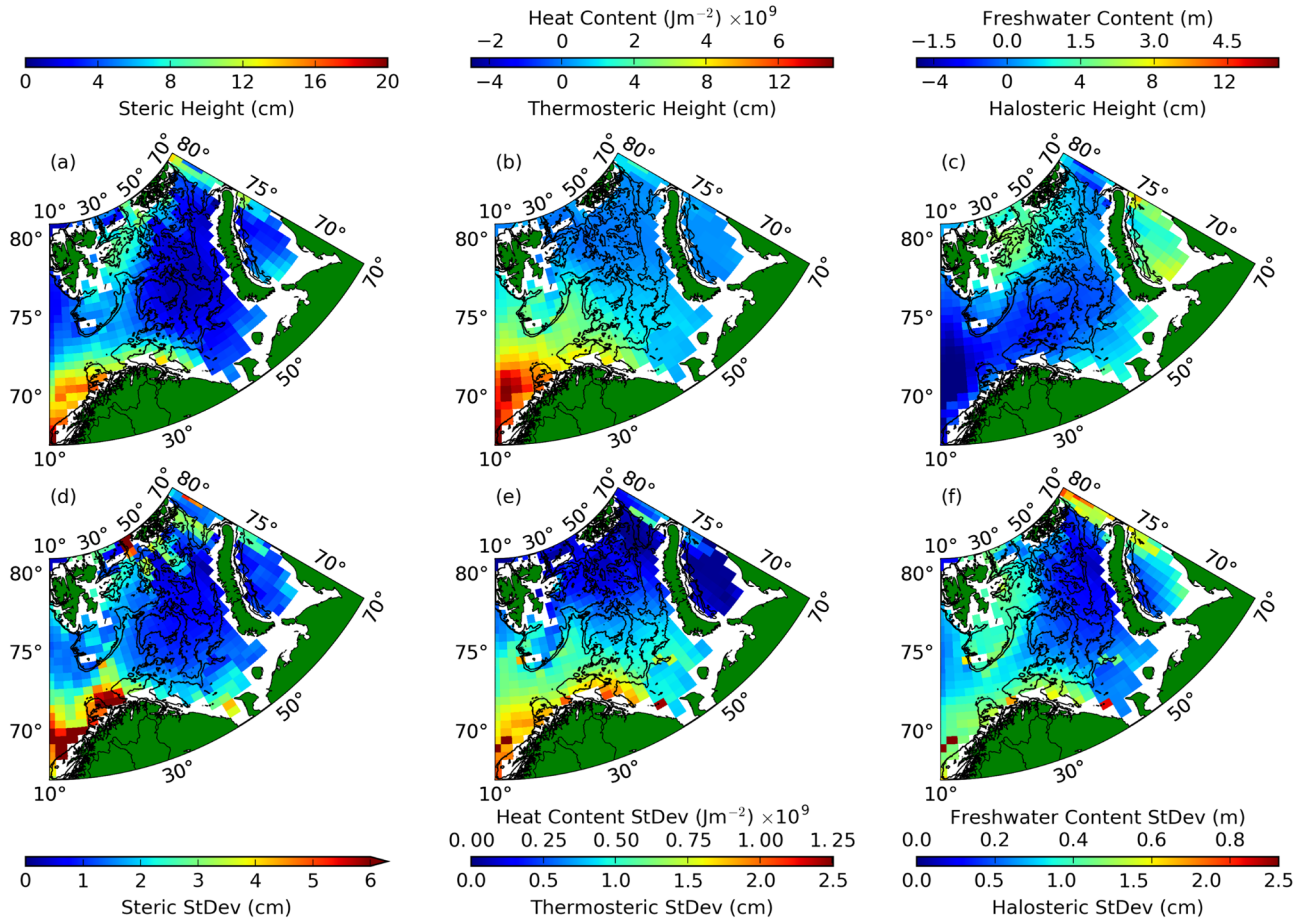

Figure 8. Same as Figure 1 but for satellite OID properties data. Note that the color scales are different to Figure 1 because of the different depth range used.

The variability in satellite OID halosteric height in the central Barents Sea is dominated by interannual variability, with only a weak seasonal cycle and an overall -0.04 cm year^{-1} decreasing halosteric height significant at 99% level (0.04 cm standard error) (Figures 5 and 9). The range of the weak seasonal cycle in satellite OID halosteric height is comparable to the estimated uncertainty value. Interannual variability is stronger and is similar to the in situ OID halosteric height (green dashed line Figure 9).

The interannual variability in halosteric height is likely to respond to surface fluxes (Ellingsen et al., 2009). The ERA-Interim atmospheric fluxes are spatially averaged within the purple box in Figure 1, and interannual variability is found using the 12 month running mean. The surface freshwater flux includes evaporation, precipitation, sea ice melt, and freeze (Ellingsen et al., 2009). In the ice-free central Barents Sea, winter evaporation outweighs precipitation, and the net precipitation in summer is due to reduced evaporation (Figure 10b). The seasonal cycle in Barents Sea evaporation is consistent with evaporation being greatest during the winter when the air-sea temperature difference is greatest. Our estimates of atmospheric freshwater flux are similar to the 0.9 mm day^{-1} found by Walsh et al. (1998) when averaged over a year, although these are larger than the ±0.6 mm day^{-1} estimated by Segtnan et al. (2011). Over our time series, there is a 0.02 mm day^{-1} year^{-1} trend in precipitation significant at 95% level (0.01 mm day^{-1} standard error). This may be decadal variability, but future climate models predict increasing rainfall over the Arctic (Bintanja & Andry, 2017). However, Aleksandrov et al. (2005) showed that between 1951 and 1992, precipitation appeared to be in decline around the northeastern Barents and Kara Seas. The trend we see in precipitation is more than compensated by the -0.05 mm day^{-1} year^{-1} trend in evaporation resulting in an overall negative trend in freshwater flux; each of these variables has a trend significant at the 99% level (0.01 mm day^{-1} standard error). At the interannual timescale atmospheric freshwater flux is not strong enough to cause interannual variability in halosteric height.

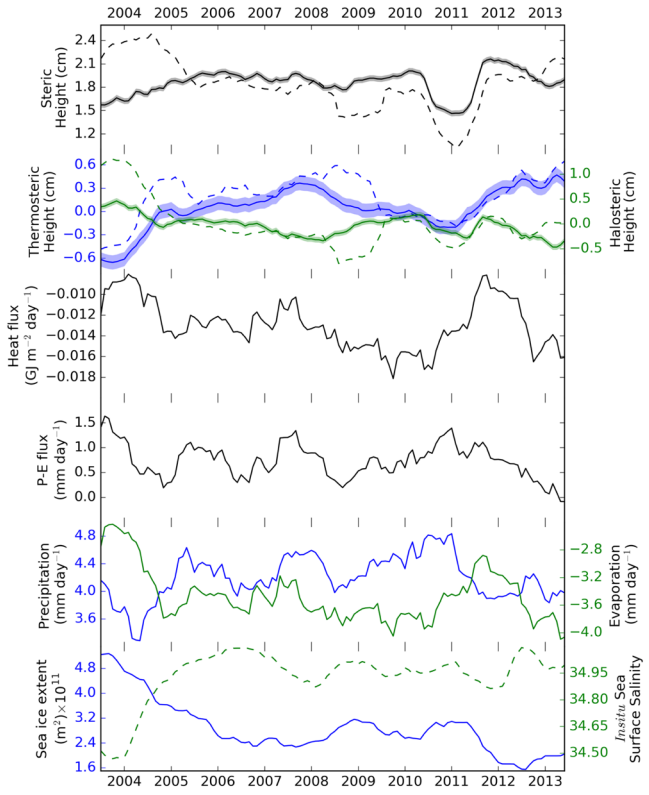

Figure 9. Time series of the OID properties used to infer BSW property variability from satellite (solid line) and in situ observations (dashed line), heat flux, precipitation, evaporation, and precipitation minus evaporation ($P-E$), and EN4 in situ sea surface salinity (SSS) averaged over the Central Basin and calculated with 12 month running mean. The time series are averaged over the Central Box (purple box in Figure 1). Standard error bars on the satellite OID data are shown by shading. The time series of the sea ice extent are averaged over the whole Barents Sea (68°N to 80°N and 10°E to 65°E).

The satellite OID halosteric interannual variability mirrors the satellite OID thermosteric interannual variability (Figure 9). Similar variability between temperature and salinity is noted between 1970 and 2000 at the Kharlov and Kanin sections in the Central Basin (Ozhigin et al., 2000). This is a feature observed northward from 59°N along the coast of Norway and may reflect the variability in mixing between relatively cool and fresh Norwegian Coastal Current water and relatively warm and salty AW (Yashayaev & Seidov, 2015). It may also reflect local variability in the influence of greater heat content reducing sea ice extent that would reduce freshwater input from melting (Figure 9). The interannual variability in OID halosteric height is similar to the interannual variability in sea ice extent. Melting of sea ice would release freshwater suggesting this could be a source of variability to halosteric height. The negative trend in satellite OID halosteric height, mentioned earlier, may be part of decadal variability but is consistent with changes in sea ice suggesting it could be part of a longer-term trend. The resulting long-term $-2.2 \times 10^{10}\,m^2\,year^{-1}$ decreasing sea ice extent (for the whole Barents Sea) is significant at 99% level ($0.18 \times 10^{10}\,m^2$ standard error) and clearly seen in the running annual means (Figure 9). The in situ SSS in this figure calculated from the Central Box also shows similar variability to the sea ice extent and halosteric height. This suggests that some of the variability in halosteric height comes from advective sea ice melt freshening the surface layer when it has greater extent. This is consistent with the Atlantification of the Barents Sea, which is believed to be driven by increasing salinity of the AW inflow and decreased freshwater from sea ice (Barton et al., 2018), that may also be abetted by a significant (at 99% level, $0.002\,GJ\,m^{-2}$ standard error) trend of -0.009 $GJ\,m^2\,year^{-1}$ in atmospheric heat flux (Figure 9) (Aleksandrov et al., 2005). Lind et al. (2018) showed that part of the Atlantification process is declining sea ice imports to the Barents Sea, which drives a major freshwater loss and weakened ocean stratification in the salinity-stratified northern Barents Sea. The ability to make observations of freshwater content, SSS and sea ice from satellite is timely, given the wider observations of changing sea ice and freshwater content in the Arctic Ocean and its importance for maintaining halocline stratification (Morison et al., 2012; Onarheim & Årthun, 2017; Polyakov et al., 2017, 2018).

OID thermosteric height determines the seasonal cycle in OID total steric height and exhibits a 0.05 cm $year^{-1}$ trend toward greater OID thermosteric height (significant at 99% level, 0.007 cm standard error) in the central Barents Sea during the study period (Figures 5 and 9). The interannual variability in satellite OID thermosteric height is similar to the in situ OID thermosteric height (blue dashed line on Figure 9). The variability between 2003 and 2009 is consistent with the variability found in temperature observations of the region by Boitsov et al. (2012) (Figure 9). OID thermosteric height is expected to respond to atmospheric heat flux into the ocean, which shows a clear seasonal cycle peaking in June but with low interannual variability (Figure 10). The offset in peak satellite OID thermosteric height in autumn (Figure 5c) relative to the peak midsummer atmospheric heat flux (Figure 10a) is entirely consistent with the ocean accumulation of heat throughout the summer. This is caused by a net gain in ocean heat from radiation and heat advection (Smedsrud et al., 2010). In our example location in Figure 3a, the increase in in situ OID heat content between September and October cannot be driven by local surface fluxes because the total surface heat flux is from the ocean to the atmosphere over this time (Smedsrud et al., 2010) (Figure 10a). Between September and October, SST decreases (Figure 3a) and the surface mixed layer is expected to deepen (Kantha & Clayson, 1994; Loeng, 1991). This suggests that the increase in heat content from September to October is lateral advection of warmer water (Figure 3a). The atmospheric heat flux also shows that more

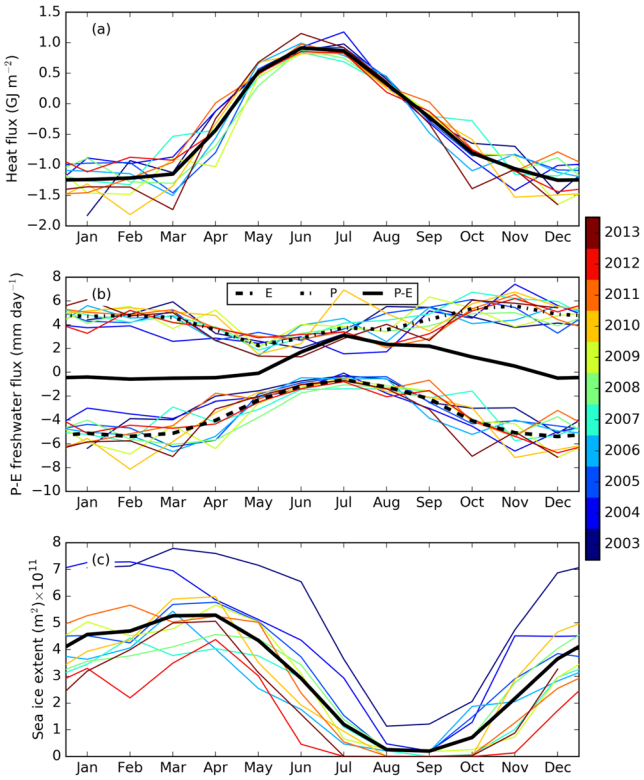

Figure 10. Same as Figure 5 but for heat flux (a). Precipitation (*P*), evaporation (*E*), and precipitation minus evaporation (*P*−*E*) are presented on (b) where positive is into the ocean. Sea ice extent is shown on (c). Note that sea ice extent is integrated over the whole Barents Sea (68°N to 80°N and 10°E to 65°E).

heat is lost in the winter than is gained in the summer and must therefore be balanced by the lateral oceanic heat transport, as suggested by Smedsrud et al. (2010).

As previously mentioned, satellite OID steric height does not show a significant trend over the study period. This is notable since we have now quantified the trends in both the satellite OID thermosteric and halosteric heights (Figure 9). Since steric height affects SSH, a trend in steric height could alter geostrophic currents. Instead, we propose that the trend in thermosteric height is balanced by the trend in halosteric height.

5. Conclusion

Heat content variability in the Barents Sea is a useful predictor for future sea ice extent (Årthun & Eldevik, 2016; Lind et al., 2018; Onarheim et al., 2015; Schlichtholz, 2019) and is, therefore, an important quantity to accurately monitor to help with understanding the sea ice-heat content coupling. Our analysis shows the potential for combining OBP, SSH, and SST satellite data to determine monthly time series of satellite upper ocean OID steric height, heat and freshwater contents for major parts of the southern Barents Sea. This is important for the local ecosystem (Eriksen et al., 2011; Oziel et al., 2017), and the southern Barents Sea is a region where SST is correlated with anomalous winter surface air temperature across Europe and Asia (Blackport et al., 2019; Hoshi et al., 2019). This builds on Volkov et al.'s (2013) analysis of steric height, thermosteric height, and halosteric height using satellite data. The satellite data offer regular, higher temporal coverage that would complement in situ profiles. Our analysis focused on the depth range between the surface and OID, which ranges from 50 to 250 m depending on the season. We regressed satellite measurements with in situ data and show that variability in the shallower summer upper layer is mixed downwards in winter making these satellite measurements characteristic of the water masses in the Barents Sea. The recent launch of GRACE-FO could make it possible to make a near real-time version of the satellite steric and halosteric heights. It may also be possible to apply these methods in other cold regions.

BSW makes up more than 50% of AIW (Maslowski et al., 2004) and entrains BSW properties (Lique et al., 2010). Our analysis shows that the main driver of the seasonal cycle in BSW steric height is variations in the heat content, which arise from a combination of advected heat and atmospheric heat flux. There is a positive trend in BSW heat content, but this trend is not found in steric height. Instead, the trend in heat content is offset by freshwater content decrease.

Data Availability Statement

Data supporting these conclusions can be obtained from web addresses in section 2.1. GRACE ocean data were processed by Don P. Chambers, supported by the NASA MEaSUREs Program, and are available online (http://grace.jpl.nasa.gov). Arctic dynamic topography data were provided by the Centre for Polar Observation and Modelling, University College London (www.cpom.ucl.ac.uk/dynamic_topography) (Armitage et al., 2016).

Acknowledgments

This project was funded through the joint UK-France PhD program by Direction Générale de l'Armement/Defence Science and Technology Laboratory (DGA/Dstl) and overseen by Carole Nahum and Timothy Clarke. Additional support for this research was provided through the Natural Environment Research Council (NERC) Changing Arctic Ocean Grant NE/R01275X/1.

References

Aksenov, Y., Bacon, S., Coward, A. C., & Nurser, A. J. G. (2010). The North Atlantic inflow to the Arctic Ocean: High-resolution model study. *Journal of Marine Systems*, *79*(1-2), 1–22. https://doi.org/10.1016/j.jmarsys.2009.05.003

Aleksandrov, Y. I., Bryazgin, N. N., Førland, E. J., Radionov, V. F., & Svyashchennikov, P. N. (2005). Seasonal, interannual and long-term variability of precipitation and snow depth in the region of the Barents and Kara seas. *Polar Research*, *24*(1-2), 69–85. https://doi.org/10.3402/polar.v24i1.6254

Armitage, T. W. K., Bacon, S., Ridout, A. L., Petty, A. A., Wolbach, S., & Tsamados, M. (2017). Arctic Ocean surface geostrophic circulation 2003–2014. *The Cryosphere*, *11*(4), 1767–1780. https://doi.org/10.5194/tc-11-1767-2017

Armitage, T. W. K., Bacon, S., Ridout, A. L., Thomas, S. F., Aksenov, Y., & Wingham, D. J. (2016). Arctic sea surface height variability and change from satellite radar altimetry and GRACE, 2003–2014. *Journal of Geophysical Research: Oceans*, *121*, 4303–4322. https://doi.org/10.1002/2015JC011579

Årthun, M., & Eldevik, T. (2016). On anomalous ocean heat transport toward the Arctic and associated climate predictability. *Journal of Climate*, *29*(2), 689–704. https://doi.org/10.1175/JCLI-D-15-0448.1

Årthun, M., Eldevik, T., Smedsrud, L. H., Skagseth, O., & Ingvaldsen, R. B. (2012). Quantifying the influence of Atlantic heat on Barents Sea ice variability and retreat. *Journal of Climate*, *25*(13), 4736–4743. https://doi.org/10.1175/JCLI-D-11-00466.1

Barton, B. I., Lenn, Y.-D., & Lique, C. (2018). Observed Atlantification of the Barents Sea causes the Polar Front to limit the expansion of winter sea ice. *Journal of Physical Oceanography*, *48*, 1849–1866. https://doi.org/10.1175/JPO-D-18-0003.1

Berrisford, P., Dee, D., Fielding, K., Fuentes, M., Kallberg, P., Kobayashi, S., & Uppala, S. (2011). The ERA-Interim archive: Version 2.0. *ERA Report Series*, *2*(1), 1–16.

Bintanja, R., & Andry, O. (2017). Towards a rain-dominated Arctic. *Nature Climate Change*, *7*(4), 263–267. https://doi.org/10.1038/nclimate3240

Blackport, R., Screen, J. A., van der Wiel, K., & Bintanja, R. (2019). Minimal influence of reduced Arctic sea ice on coincident cold winters in mid-latitudes. *Nature Climate Change*, *9*, 697–704. https://doi.org/10.1038/s41558-019-0551-4

Boitsov, V. D., Karsakov, A. L., & Trofimov, A. G. (2012). Atlantic water temperature and climate in the Barents Sea, 2000–2009. *ICES Journal of Marine Science*, *69*(5), 833–840. https://doi.org/10.1093/icesjms/fst075

Carmack, E. C. (2007). The alpha/beta ocean distinction: A perspective on freshwater fluxes, convection, nutrients and productivity in high-latitude seas. *Deep-Sea Research Part II: Topical Studies in Oceanography*, *54*(23-26), 2578–2598. https://doi.org/10.1016/j.dsr2.2007.08.018

Chambers, D. P., & Bonin, J. A. (2012). Evaluation of Release-05 GRACE time-variable gravity coefficients over the ocean. *Ocean Science*, *8*(5), 859–868. https://doi.org/10.5194/os-8-859-2012

Chambers, D. P., & Willis, J. K. (2010). A global evaluation of ocean bottom pressure from GRACE, OMCT, and steric-corrected altimetry. *Journal of Atmospheric and Oceanic Technology*, *27*(8), 1395–1402. https://doi.org/10.1175/2010JTECHO738.1

Chepurin, G. A., & Carton, J. A. (2012). Subarctic and Arctic sea surface temperature and its relation to ocean heat content 1982–2010. *Journal of Geophysical Research*, *117*, C06019. https://doi.org/10.1029/2011JC007770

Donlon, C. J., Martin, M., Stark, J., Roberts-Jones, J., Fiedler, E., & Wimmer, W. (2012). The Operational Sea Surface Temperature and Sea Ice Analysis (OSTIA) system. *Remote Sensing of Environment*, *116*, 140–158. https://doi.org/10.1016/j.rse.2010.10.017

Ellingsen, I., Slagstad, D., & Sundfjord, A. (2009). Modification of water masses in the Barents Sea and its coupling to ice dynamics: A model study. *Ocean Dynamics*, *59*(6), 1095–1108. https://doi.org/10.1007/s10236-009-0230-5

Eriksen, E., Bogstad, B., & Nakken, O. (2011). Ecological significance of 0-group fish in the Barents Sea ecosystem. *Polar Biology*, *34*(5), 647–657. https://doi.org/10.1007/s00300-010-0920-y

Font, J., Boutin, J., Reul, N., Spurgeon, P., Ballabrera-Poy, J., Chuprin, A., et al. (2013). SMOS first data analysis for sea surface salinity determination. *International Journal of Remote Sensing*, *34*(9-10), 3654–3670. https://doi.org/10.1080/01431161.2012.716541

Giglio, D., Roemmich, D., & Cornuelle, B. (2013). Understanding the annual cycle in global steric height. *Geophysical Research Letters*, *40*, 4349–4354. https://doi.org/10.1002/grl.50774

Giles, K. A., Laxon, S. W., Ridout, A. L., Wingham, D. J., & Bacon, S. (2012). Western Arctic Ocean freshwater storage increased by wind-driven spin-up of the Beaufort Gyre. *Nature Geoscience*, *5*(3), 194–197. https://doi.org/10.1038/ngeo1379

Gill, A. E., & Niiler, P. P. (1973). The theory of the seasonal variability in the ocean. *Deep-Sea Research and Oceanographic Abstracts*, *20*(2), 141–177. https://doi.org/10.1016/0011-7471(73)90049-1

Gouretski, V., & Reseghetti, F. (2010). On depth and temperature biases in bathythermograph data: Development of a new correction scheme based on analysis of a global ocean database. *Deep-Sea Research Part I: Oceanographic Research Papers*, *57*(6), 812–833. https://doi.org/10.1016/j.dsr.2010.03.011

Hoshi, K., Ukita, J., Honda, M., Nakamura, T., Yamazaki, K., Miyoshi, Y., & Jaiser, R. (2019). Weak stratospheric polar vortex events modulated by the Arctic sea-ice loss. *Journal of Geophysical Research: Atmospheres*, *124*, 858–869. https://doi.org/10.1029/2018JD029222

IOC, SCOR, & IAPSO (2010). The International Thermodynamic Equation of Seawater—2010: Calculation and use of thermodynamic properties. *Intergovernmental Oceanographic Commission, Manuals and Guides*, *No. 56*(UNESCO), 196. Retrieved from http://www.teos-10.org/

Kantha, L. H., & Clayson, C. A. (1994). An improved mixed layer model for geophysical applications. *Journal of Geophysical Research*, *99*(C12), 25,235–25,266. https://doi.org/10.1029/94JC02257

Laxon, S. (1994). Sea ice altimeter processing scheme at the EODC. *International Journal of Remote Sensing*, *15*(4), 915–924.

Lind, S., Ingvaldsen, R. B., & Furevik, T. (2018). Arctic warming hotspot in the northern Barents Sea linked to declining sea-ice import. *Nature Climate Change*, *8*, 634–639. https://doi.org/10.1038/s41558-018-0205-y

Lique, C., & Steele, M. (2013). Seasonal to decadal variability of Arctic Ocean heat content: A model-based analysis and implications for autonomous observing systems. *Journal of Geophysical Research: Oceans*, *118*, 1673–1695. https://doi.org/10.1002/jgrc.20127

Lique, C., Treguier, A. M., Blanke, B., & Grima, N. (2010). On the origins of water masses exported along both sides of Greenland: A Lagrangian model analysis. *Journal of Geophysical Research*, *115*, C05019. https://doi.org/10.1029/2009JC005316

Loeng, H. (1991). Features of the physical oceanograpic conditions of the Barents Sea. *Polar Research*, *10*(1), 5–18. https://doi.org/10.1111/j.1751-8369.1991.tb00630.x

Long, Z., & Perrie, W. (2017). Changes in ocean temperature in the Barents Sea in the twenty-first century. *Journal of Climate*, *30*(15), 5901–5921. https://doi.org/10.1175/JCLI-D-16-0415.1

Maslowski, W., Marble, D., Walczowski, W., Schauer, U., Clement, J. L., & Semtner, A. J. (2004). On climatological mass, heat, and salt transports through the Barents Sea and Fram Strait from a pan-Arctic coupled ice-ocean model simulation. *Journal of Geophysical Research*, *109*, C03032. https://doi.org/10.1029/2001JC001039

McDougall, T. J. (1987). Neutral surfaces. *Journal of Physical Oceanography*, *17*, 1950–1964.

Moat, B., Josey, S., & Sinhu, B. (2014). Impact of Barents Sea winter air-sea exchanges on Fram Strait dense water transport. *Journal of Geophysical Research: Oceans*, *119*, 1009–1021. https://doi.org/10.1002/2013JC009220

Morison, J., Kwok, R., Peralta-Ferriz, C., Alkire, M., Rigor, I., Andersen, R., & Steele, M. (2012). Changing Arctic Ocean freshwater pathways. *Nature*, *481*(7379), 66–70. https://doi.org/10.1038/nature10705

Olmedo, E., Gabarró, C., González-Gambau, V., Martínez, J., Ballabrera-Poy, J., Turiel, A., et al. (2018). Seven years of SMOS sea surface salinity at high latitudes: Variability in Arctic and sub-Arctic regions. *Remote Sensing*, *10*(11), 1–24. https://doi.org/10.3390/rs10111772

Onarheim, I. H., & Årthun, M. (2017). Toward an ice-free Barents Sea. *Geophysical Research Letters*, *44*, 8387–8395. https://doi.org/10.1002/2017GL074304

Onarheim, I. H., Eldevik, T., Årthun, M., Ingvaldsen, R. B., & Smedsrud, L. H. (2015). Skillful prediction of Barents Sea ice cover. *Geophysical Research Letters*, *42*, 5364–5371. https://doi.org/10.1002/2015GL064359.Abstract

Ozhigin, V. K., Trofimov, A. G., & Ivshin, V. A. (2000). The Eastern Basin Water and currents in the Barents Sea. In *ICES Annual Science Conference 2000 Theme Session L: North Atlantic Processes* (pp. 1–19). Bruges, Belgium.

Oziel, L., Neukermans, G., Ardyna, M., Lancelot, C., Tison, J.-L., Wassmann, P., et al. (2017). Role for Atlantic inflows and sea ice loss on shifting phytoplankton blooms in the Barents Sea. *Journal of Geophysical Research: Oceans*, *122*, 5121–5139. https://doi.org/10.1002/2016JC012582.Received

Oziel, L., Sirven, J., & Gascard, J. C. (2016). The Barents Sea frontal zones and water masses variability (1980–2011). *Ocean Science*, *12*(1), 169–184. https://doi.org/10.5194/os-12-169-2016

Peralta-Ferriz, C., Morison, J. H., & Wallace, J. M. (2016). Proxy representation of Arctic ocean bottom pressure variability: Bridging gaps in GRACE observations. *Geophysical Research Letters*, *43*, 9183–9191. https://doi.org/10.1002/2016GL070137

Peralta-Ferriz, C., Morison, J. H., Wallace, J. M., Bonin, J. A., & Zhang, J. (2014). Arctic Ocean circulation patterns revealed by GRACE. *Journal of Climate*, *27*(4), 1445–1468. https://doi.org/10.1175/JCLI-D-13-00013.1

Petoukhov, V., & Semenov, V. A. (2010). A link between reduced Barents-Kara sea ice and cold winter extremes over northern continents. *Journal of Geophysical Research*, *115*, D21111. https://doi.org/10.1029/2009JD013568

Polyakov, I. V., Pnyushkov, A. V., Alkire, M. B., Ashik, I. M., Baumann, T. M., Carmack, E. C., et al. (2017). Greater role for Atlantic inflows on sea-ice loss in the Eurasian Basin of the Arctic Ocean. *Science*, *291*(April), 285–291. https://doi.org/10.1126/science.aai8204

Polyakov, I. V., Pnyushkov, A. V., & Carmack, E. C. (2018). Stability of the Arctic halocline: A new indicator of Arctic climate change. *Environmental Research Letters*, *13*(12), 1–8. https://doi.org/10.1088/1748-9326/aaec1e

Regan, H. C., Lique, C., & Armitage, T. W. K. (2019). The Beaufort Gyre extent, shape, and location between 2003 and 2014 from satellite observations. *Journal of Geophysical Research: Oceans*, *124*, 844–862. https://doi.org/10.1029/2018JC014379

Reynolds, R. W. (1988). A real-time global sea surface temperature analysis. *Journal of Climate*, *1*, 75–86. https://doi.org/10.1175/1520-0442(1993)006<0114:airtgs>2.0.co;2

Richter, K., Nilsen, J. E. O., & Drange, H. (2012). Contributions to sea level variability along the Norwegian coast for 1960–2010. *Journal of Geophysical Research*, *117*, C05038. https://doi.org/10.1029/2011JC007826

Roquet, F., Madec, G., McDougall, T. J., & Barker, P. M. (2015). Accurate polynomial expressions for the density and specific volume of seawater using the TEOS-10 standard. *Ocean Modelling*, *90*, 29–43. https://doi.org/10.1016/j.ocemod.2015.04.002

Sakumura, C., Bettadpur, S., & Bruinsma, S. (2014). Ensemble prediction and intercomparison analysis of GRACE time-variable gravity field models. *Geophysical Research Letters*, *41*, 1389–1397. https://doi.org/10.1002/2013GL058632

Schauer, U., Loeng, H., Rudels, B., Ozhigin, V. K., & Dieck, W. (2002). Atlantic Water flow through the Barents and Kara Seas. *Deep-Sea Research Part I: Oceanographic Research Papers*, *49*(12), 2281–2298. https://doi.org/10.1016/S0967-0637(02)00125-5

Schauer, U., Muench, R. D., Rudels, B., & Timokhov, L. (1997). Impact of eastern Arctic shelf waters on the Nansen Basin intermediate layers. *Journal of Geophysical Research*, *102*(C2), 3371. https://doi.org/10.1029/96JC03366

Schlichtholz, P. (2019). Subsurface ocean flywheel of coupled climate variability in the Barents Sea hotspot of global warming. *Scientific Reports*, *9*(1), 1–16. https://doi.org/10.1038/s41598-019-49965-6

Segtnan, O. H., Furevik, T., & Jenkins, A. D. (2011). Heat and freshwater budgets of the Nordic seas computed from atmospheric reanalysis and ocean observations. *Journal of Geophysical Research*, *116*, C11003. https://doi.org/10.1029/2011JC006939

Skagseth, O. (2008). Recirculation of Atlantic Water in the western Barents Sea. *Geophysical Research Letters*, *35*, L11606. https://doi.org/10.1029/2008GL033785

Smedsrud, L. H., Ingvaldsen, R., Nilsen, J. E. O., & Skagseth, O. (2010). Heat in the Barents Sea: Transport, storage, and surface fluxes. *Ocean Science*, *6*(1), 219–234. https://doi.org/10.5194/os-6-219-2010

Steele, M., & Ermold, W. (2007). Steric sea level change in the Northern Seas. *Journal of Climate*, *20*, 403–417.

Stewart, K. D., & Haine, T. W. N. (2016). Thermobaricity in the transition zones between alpha and beta oceans. *Journal of Physical Oceanography*, *46*(6), 1805–1821. https://doi.org/10.1175/JPO-D-16-0017.1

Swart, S., Speich, S., Ansorge, I. J., & Lutjeharms, J. R. E. (2010). An altimetry-based gravest empirical mode south of Africa: 1. Development and validation. *Journal of Geophysical Research*, *115*, C03002. https://doi.org/10.1029/2009JC005299

Volkov, D. L., Landerer, F. W., & Kirillov, S. A. (2013). The genesis of sea level variability in the Barents Sea. *Continental Shelf Research*, *66*, 92–104. https://doi.org/10.1016/j.csr.2013.07.007

Volkov, D. L., & Pujol, M. I. (2012). Quality assessment of a satellite altimetry data product in the Nordic, Barents, and Kara seas. *Journal of Geophysical Research*, *117*, C03025. https://doi.org/10.1029/2011JC007557

Wahr, J., Molenaar, M., & Bryan, F. (1998). Time variability of the Earth's gravity field: Hydrological and oceanic effects and their possible detection using GRACE. *Journal of Geophysical Research*, *103*(B12), 30,205–30,229.

Walsh, J. E., Kattsov, V., Portis, D., & Meleshko, V. (1998). Arctic precipitation and evaporation: Model results and observational estimates. *Journal of Climate*, *11*, 72–87.

Weatherall, P., Marks, K. M., Jakobsson, M., Schmitt, T., Tani, S., Arndt, J. E., et al. (2015). A new digital bathymetric model of the world's oceans. *Earth and Space Science*, *2*, 331–345. https://doi.org/10.1002/2015EA000107.Received

Yashayaev, I., & Seidov, D. (2015). The role of the Atlantic Water in multidecadal ocean variability in the Nordic and Barents Seas. *Progress in Oceanography*, *132*(December 2014), 68–127. https://doi.org/10.1016/j.pocean.2014.11.009